ACS OMEGA

http://pubs.acs.org/journal/acsodf

Article

Progressive Damage Analysis for Spherical Electrode Particles with Different Protective Structures for a Lithium-Ion Battery

Qi Liu, J. G. Wang,* and Bowen Hu

Cite This: *ACS Omega* 2023, 8, 7492−7506

Read Online

ACCESS | Metrics & More | Article Recommendations

ABSTRACT: Charge−discharge in a lithium-ion battery may produce electrochemical adverse reactions in electrodes as well as electrolytes and induce local inhomogeneous deformation and even mechanical fracture. An electrode may be a solid core−shell structure, hollow core−shell structure, or multilayer structure and should maintain good performance in lithium-ion transport and structural stability in charge−discharge cycles. However, the balance between lithium-ion transport and fracture prevention in charge−discharge cycles is still an open issue. This study proposes a novel binding protective structure for lithium-ion battery and compares its performance during charge−discharge cycles with unprotective structure, core−shell structure and hollow structure. First, both solid and hollow core−shell structures are reviewed, and their analytical solutions of radial and hoop stresses are derived. Then, a novel binding protective structure is proposed to well-balance lithium-ionic permeability and structural stability. Third, the pros and cons of the performance at the outer structure are investigated. Both analytical and numerical results show that the binding protective structure serves with great fracture-proof effectiveness and high lithium-ion diffusion rate. It has better ion permeability than solid core−shell structure but worse structural stability than shell structure. A stress surge is observed at the binding interface with an order of magnitude usually higher than that of the core−shell structure. The radial tensile stress at interface may more easily induce interfacial debonding than superficial fracture.

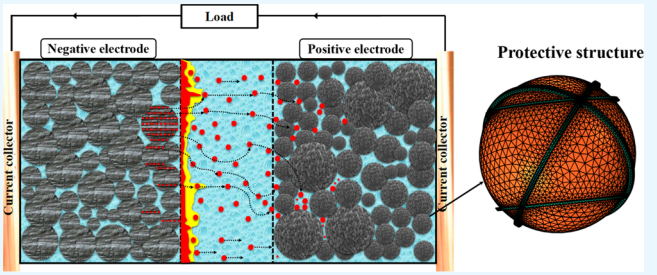

1. INTRODUCTION

Lithium-ion battery (LIB) is the most potential energy-storage unit due to its features of high energy density, high working voltage, and long cycle life. Due to its high performance, LIB is ubiquitous ranging from small-scale portable electronic products like cellphones and laptops to large-scale rechargeable vehicles.[1−3] Driven by the prosperous new energy market, LIB technology has made a rapid improvement in both ion transport and structural stability.[4,5] However, the safety performance of LIB is still a non-negligible disadvantage.

The fracture of active electrodes induces capacity decay and power fading, sometimes even explosion and fire accidents.[6] The structure safety of LIB depends on many factors such as operation environment, abuse tolerance and composition properties. Its safety and aging mechanism are directly affected by multiphysical couplings in thermal, electrochemical, mechanical and diffusion processes.[7−10] That is, the ionic insertion or extraction occurs in the charging and discharging process over thousands of lithiation and delithiation cycles. This expansion/contraction leads to the inhomogeneous deformation of electrode particles, which generates unbearable large local strain and further triggers progressive damage and even fracture.[11] Meantime, electrode and electrolyte have the electrochemical reaction at the solid−liquid interface, thus forming a solid electrolyte interface (SEI). Over the cycles, SEI experiences formation, growth and dissolution. In summary, the multiphysical coupling induced inhomogeneous deformation of electrode particles in the charging and discharging process is critical to the safety and aging of lithium-ion battery.

The fracture mechanism of electrodes varies with the mechanical properties of electrode and operation mode. Generally, conductive materials for battery anodes are graphite, silicon, germanium, tin and so on. Among the anode materials, silicon is considered as one prospective alternative material when compared with the broadly used graphite. Based on the properties like the superior known charge capacity (4200 mAh·g^{-1}) and the low discharge potential, silicon is manufactured into various forms of electrodes to improve the LIB performance.[12] However, silicon as a host material in lithiation may have a high-volume change rate, which can reach 400% upon the cycle. This change rate of volume may trigger an excessive local strain and result in the pulverization of the electrode and severe

Received: October 11, 2022
Accepted: February 3, 2023
Published: February 17, 2023

https://doi.org/10.1021/acsomega.2c06560
ACS Omega 2023, 8, 7492−7506

fade of energy density.[13,14] Hence, the LIB should have a safety strategy to avoid this potential fracture in the material.

Protective coating is an effective safety strategy to prevent the electrode from chemical erosion and mechanical fractures. Usually, a core−shell structure is designed to protect electrode materials. That is, a layer of protective material is coated on the surface of the active electrode, forming a core−shell structure. This structure has three advantages: (1) Avoid the direct contact between the active electrode and the electrolyte solution and thus reduce electrochemical side reactions;[15,16] (2) Combine the advantages of multiple materials within a composite structure. This can improve the overall physical-chemical properties;[17] (3) Structurally constrain the volumetric deformation of the active electrode, thus inducing local strain. In the core−shell structure, the tensile stress on the surface of the particles is the main traction leading to fracture when the electrode is swelling during the ion storage and withdrawal cycle.[18,19] Particularly, the shell constrains the deformation of the core and transmits the tensile stress to the surface of the shell. Therefore, the fracture indicators of the core−shell structure are transformed into: (1) Tensile stress on the shell surface during the lithium insertion process. (2) Radial stress on the core−shell interface during the ion lithium extraction process.[20,21] Once interfacial delamination or surface decrepitation occurs, the elaborately optimized structure will lose all the working effectiveness.[22,23] Thus, the feasibility and applicability of coating structure is critical to the LIB safety and should be carefully investigated.

Core−shell structures have been widely developed in the battery industry for the notable enhancement of LIB performance. For example, a core−shell structure is composed of a lithium cobalt oxide ($LiCoO_2$) core and an aluminum phosphate ($AlPO_4$) shell.[24] This structure allows the electrode to be charged and discharged stably under high temperature and high cutoff voltage. A porous carbon coated core/shell Fe_3O_4@carbon structure presents excellent electrochemical properties (839 mA·h·g^{-1} at 0.3A·g^{-1} after 200 cycles) and rate capacities. At the same time, the carbon constrains the excessive deformation of the core.[25] Core/shell $(Ni_{0.5}Co_{0.5})_9S_8$@NC structure encapsulated in the nitrogen-doped carbon coating shows the remarkable properties including a capacity of 724 mAh·g^{-1} at 0.5 A·g^{-1} cycled for 80 times, attractive cycling stability and appealing rate capability.[26] A further extension is the hollow core−shell structure which is suitable for the materials with larger volumetric deformation such as silicon. The hollow part of the structure accommodates the volumetric deformation of the electrode, while the shell protects the active electrode. Electrode materials can be also fabricated into electrodes with nanowires,[27] nanotube,[28,29] thin nanofilms,[30] and nano porous structures[31] to improve the electrode stability. Silicon nanowires are taken as an example, the active material is manufactured into closely arranged equal-length cylindrical electrodes and fixed on the electrode current collector. This structure allows the volumetric deformation of a single silicon nanowire. Hence, the core−shell protection has a good practical application.

Several theoretical models in continuum mechanics have been proposed to evaluate the safety performance. The diffusion induced stress (DIS) model, which was first proposed in 1961,[32] describes the force condition of the electrode in the electrolyte by analogy with temperature stress. On this basis, a fully coupling diffusion-deformation theory was developed and has been applied to the large elastoplastic deformation. The influence of plasticity in electrochemical performance was investigated and the plastic flow was found to reduce the reaction potential for lithiation.[33] Anand[34] formulated a unified framework to couple the large elastoplastic deformation and the Chan-Hilliard-type species diffusion. This framework can account for the evolution of stress caused by the diffusion of lithium ions in the electrodes. Continuum method for crack evolution analysis was first applied to describe the propagation of the crack during fracture process in the amorphous material.[35] The phase field model was applied to simulate the crack propagation. The influence of electrode particle size and initial crack on fracturing was explored. Wang et al.[36] derived a constitutive relation by combining the strain gradient plasticity and electrochemical relation of LIB electrode. Validation and simulation showed that their novel model agrees well with the classic linear elastic model in the most positions apart from the interface. Zhao et al.[37] used dimensional analysis to derive the expression of fracture energy release rate which is suitable for the core−shell structure. Later they analyzed the influence of variables such as the thickness of a shell on fracture failure. They believed that the interfacial delamination precedes the fracture of a shell. However, these studies only focus on the numerical simulation of a single structure. They rarely investigate the performance of multiple structure types comparatively.

In this paper, we will propose a binding protective structure, build solid core−shell, hollow core−shell protective structures and unprotected structure for electrode and numerically evaluate their performance on the balance between permeability and fracture prevention. Their performance in both fracture prevention and ion transmission are investigated through numerical simulations within the *COMSOL Multiphysics*, a PDE solver by FEM. This paper is organized as follows: In Section 2, the mathematical equations for the coupling of ion diffusion and mechanical deformation in protective structures are developed and their analytical solutions are derived. In Section 3, the 3D model setup and validation for numerical simulations are discussed. In Section 4, the performance of four structures in deformation, stress and ion transmission is compared. Conclusions are drawn in Section 5.

2. MATHEMATICAL MODEL FOR PROTECTION STRUCTURE

The charging and discharging process of lithium-ion electrode involves multiphysical processes in different protective structures. This paper discusses unprotected structure and three protective structures of spherical electrodes: Solid core−shell structure, grid binding structure, and hollow core−shell structure. Their structures are shown in Figure 1. Their governing equations, initial and boundary conditions are presented, and their analytical solutions are derived. In these models, the core and shell are all isotropic, linear and elastic. The model geometry and material parameters are listed in Table 1. These values of physical quantities are provided by the software.

2.1. Ion Diffusion during Charging and Discharging Process. The ion diffusion is assumed to follow the Fick's second law. The change of lithium-ion concentration in a porous electrode is related to its concentration gradient as

$$\frac{\partial C}{\partial t} = \frac{D}{r^2}\frac{\partial}{\partial r}\left(r^2\frac{\partial C}{\partial r}\right) \quad (1)$$

where D is the diffusion coefficient in the porous electrode and C (r, t) is the concentration at the radius r and time t.

https://doi.org/10.1021/acsomega.2c06560
ACS Omega 2023, 8, 7492−7506

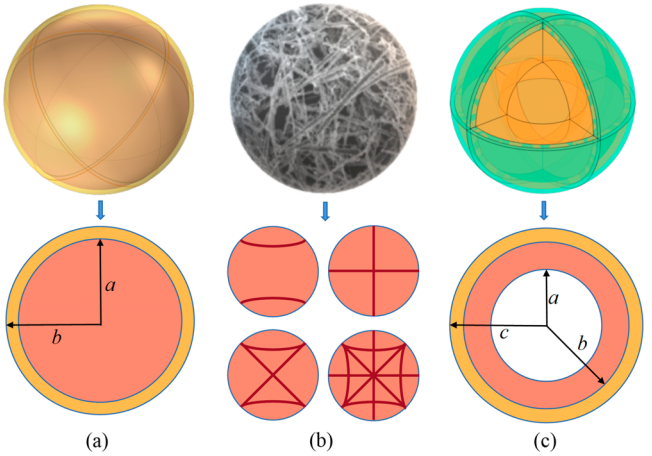

Figure 1. Model geometry of the protective structure electrode ((a) Solid core−shell structure, where the shell isolates the electrode and electrolyte and prevents electrode breakage; (b) Binding structure, which takes into account the two advantages of structure protection for concentration transmission; (c) Hollow core−shell structure, which is suitable for materials with large volume change rate.).

Table 1. Computational Parameters in Numerical Simulations

Parameters	Electrode model	References
Faraday constant, *Fa* (A·s/mol)	96485.3145	41
Gas constant, *R* (J/mol·K)	8.314	41
Diffusion coefficient, *D* (m^2/s)	2×10^{-14}	42
Ambient temperature, *T* (K)	300	Estimated
Partial molar volume of ions in the electrode, Ω (m^3)	3.42×10^{-6}	43
Charging current density, *in* (A/m^2)	2	Estimated
Solid electrode radius, $R_{sradius}$ (μm)	4	41
The thickness of shell in solid core shell model, l_s (μm)	0.2	Estimated
Partial molar volume of ions in the spherical shell, $Ω_s$ (m^3)	5.3×10^{-6}	44
The thickness of binding, l_b (μm)	0.2	Estimated
Concentration stress in the electrode, σ_c	Ω·E·c/(3−3·μ)	Expression
Variable diffusion coefficient in the electrode	$D \cdot \exp(\Omega \cdot \sigma_c / R/T)$	Expression
Initial concentration value	*in*/*Fa*	Expression
Variable diffusion coefficient in the spherical shell	$D \cdot \exp(\Omega_s \cdot \sigma_s / R/T)$	Expression
Concentration stress in the spherical shell, σ_s	$\Omega_s \cdot E_s \cdot c/(3-3 \cdot \mu_s)$	Expression
Elastic modulus of Al_2O_3 shell, E_s (GPa)	375	45
elastic modulus of Si core, *E* (GPa)	15	44
Poisson's ratio of the Al_2O_3 shell, μ_s	0.22	45
Poisson's ratio of the Si core, μ	0.3	44
Critical energy of interface debonding, Γ_d ($J \cdot m^{-2}$)	40	39
Critical energy of surface fracture, Γ_f ($J \cdot m^{-2}$)	10	39

This equation expresses the conservation of matter lithium. Under constant voltage charge of the battery, its boundary conditions are

$$\begin{aligned} C(r, 0) &= C_0, \quad \text{for } 0 \le r \le R \\ C(R, t) &= C_R, \quad \text{for } t \ge 0 \\ C(0, t) &= \text{finite}, \quad \text{for } t \ge 0 \end{aligned} \tag{2}$$

The average concentration on the surface $C_{av}(R)$ and inside $C_{av}(r)$ are obtained by[38]

$$\begin{cases} \dfrac{C(r, t) - C_0}{C_R - C_0} = 1 + 2\sum_{n=1}^{\infty} \dfrac{(-1)^n}{n\pi x} \sin(n\pi x) e^{-n^2\pi^2\tau} \\ \dfrac{C_{av}(r) - C_0}{C_R - C_0} = 1 + \dfrac{6}{x^3} \sum_{n=1}^{\infty} \dfrac{(-1)^n}{n^3\pi^3} [\sin(n\pi x) - (n\pi x)\cos(n\pi x)] e^{-n^2\pi^2\tau} \\ \dfrac{C_{av}(R) - C_0}{C_R - C_0} = 1 - 6\sum_{n=1}^{\infty} \dfrac{1}{n^2\pi^2} e^{-n^2\pi^2\tau} \end{cases} \tag{3}$$

where $x = r/R$ and $\tau = Dt/R^2$. C_0 and C_R represent the concentration at the center and surface of the sphere, respectively.

2.2. Solid Core−Shell Structure. The solid core−shell model is shown in Figure 1(a). The radius of the core is *a*, and the thickness of the shell is *b*−*a*. The microelements inside the structure are subjected to a triaxial stress (σ_r, σ_T, σ_T), where σ_r is the radial stress and σ_T is the hoop stress. This is a spherically symmetrical electrode particle. Its mechanical equilibrium equation is

$$\frac{\partial \sigma_r}{\partial r} + 2\frac{\partial \sigma_r - \partial \sigma_T}{r} = 0 \tag{4}$$

During the charging and discharging process of a battery, lithiation and delithiation will cause particle deformation. This deformation is measured by the sorption-induced volumetric strain and directly related to the lithium concentration $C(r,t)$ as[32]

$$\varepsilon_c = \frac{\Omega C}{3} \tag{5}$$

where Ω is the partial molar volume of lithium in the host material.

The constitutive equation for the deformation-concentration coupling is expressed as

$$\begin{aligned} \varepsilon_r &= \frac{1}{E}(\sigma_r - 2\nu\sigma_T) + \frac{\Omega C}{3} \\ \varepsilon_T &= \frac{1}{E}[(1 - \nu)\sigma_T - \nu\sigma_r] + \frac{\Omega C}{3} \end{aligned} \tag{6}$$

where *E* is the Young's modulus and *ν* is the Poisson ratio.

The displacement at the center of the sphere is assumed to be zero and the stress on the surface of the sphere is zero. Both displacement and stress are continuous at the core−shell interface. Therefore,

$$\begin{aligned} u_c(r = a) &= u_s(r = a) \\ \sigma_{r,c}(r = a) &= \sigma_{r,s}(r = a) \\ u_c(r = 0) &= 0 \\ \sigma_{r.s}(r = b) &= 0 \end{aligned} \tag{7}$$

The solutions for the radial stress σ_r at the core−shell interface and the hoop stress σ_T on the surface are[38]

$$\begin{cases} \sigma_T^s = -\dfrac{3a^3}{2(b^3 - a^3)}\sigma_T^{cs} + \dfrac{\Omega_s E_s}{3(1-\nu_s)}\left[\dfrac{1}{b^3 - a^3}\left(2 + \left(\dfrac{a}{b}\right)^3\right)\int_a^b C_s(r) r^2 dr + \dfrac{1}{r^3}\int_a^b C_s(r) r^2 dr - C_s(r)\right] \\ \sigma_r^{cs} = \dfrac{2E_c E_s}{a^3} \dfrac{\Omega_s \int_a^b C_s(r) r^2 dr - \left[\left(\dfrac{b}{a}\right)^3 - 1\right]\Omega_c \int_0^a C_c(r) r^2 dr}{\left(\dfrac{b}{a}\right)^3 \left[E_c(1+\nu_s) + 2E_s(1-2\nu_c)\right] + 2\left[E_c(1-2\nu_s) - E_s(1-2\nu_c)\right]} \end{cases} \tag{8}$$

https://doi.org/10.1021/acsomega.2c06560
ACS Omega 2023, 8, 7492−7506

The average concentration is $C_{av}(r,t) = (3/r^3)\int_0^r C(r,t)r^2dr$. Then, eq 3 can be substituted into eq 8 to obtain the analytical solutions as

$$\begin{cases} \sigma_r^{cs} = \dfrac{2E_cE_s}{a^3}\dfrac{1}{\left(\frac{b}{a}\right)^3\left[E_c(1+\nu_s)+2E_s(1-2\nu_c)\right]+2\left[E_c(1-2\nu_s)-E_s(1-2\nu_c)\right]} \\ \quad \left\{\Omega_s\left(6\sum_{n=1}^{\infty}\frac{1}{n^2\pi^2}e^{-n^2\pi^2\tau}-\frac{6}{x_b^3}\sum_{n=1}^{\infty}\frac{(-1)^n}{n^3\pi^3}[\sin(n\pi x_b)-(n\pi x_b)\cos(n\pi x_b)]e^{-n^2\pi^2\tau}\right)(C_R-C_0)+C_0\Omega_s+\right. \\ \quad \left.\left[\left(1+\frac{6}{x_a^3}\sum_{n=1}^{\infty}\frac{(-1)^n}{n^3\pi^3}[\sin(n\pi x_a)-(n\pi x_a)\cos(n\pi x_a)]e^{-n^2\pi^2\tau}\right)(C_R-C_0)+C\right]\left[\left(\frac{b}{a}\right)^3\Omega_c-(\Omega_c+\Omega_s)\right]\right\} \\ \sigma_T^s = -\dfrac{3a^3}{2(b^3-a^3)}\sigma_T^{cs}+\dfrac{\Omega_sE_s}{3(1-\nu_s)}\left\{\left[\frac{1}{b^3-a^3}\left(2+\left(\frac{a}{b}\right)^3\right)+\frac{1}{r^3}\right]\right. \\ \quad \left[\left(6\sum_{n=1}^{\infty}\frac{1}{n^2\pi^2}e^{-n^2\pi^2\tau}-\frac{6}{x_b^3}\sum_{n=1}^{\infty}\frac{(-1)^n}{n^3\pi^3}[\sin(n\pi x_b)-(n\pi x_b)\cos(n\pi x_b)]e^{-n^2\pi^2\tau}\right)(C_R-C_0)\right] \\ \quad \left.-\left(1+2\sum_{n=1}^{\infty}\frac{(-1)^n}{n\pi x}\sin(n\pi x)e^{-n^2\pi^2\tau}\right)(C_R-C_0)-C_0\right\} \end{cases} \quad (9)$$

This formula shows that the stress increases with time and concentration for given radius and core thickness.

2.3. Grid Binding Structure. The shell in the core−shell structure should be carefully designed to meet different functions. For example, the shell should be so designed that ion migration easily moves in/out and its structure is of lightweight and strong stiffness. Actually, the shell is to provide a constraint on the swelling deformation. We propose a grid binding structure to replace the core−shell structure. The grid binding structure can not only impose constraints on the deformation of active electrode, but also can reduce the requirements on the permeability of shell material. Particularly, ions can move freely in the grid.

A grid binding structure is shown in Figure 1b. The thin nanowires are bound on the outer surface of the sphere. The binding constraint makes the structure statically indeterminate. In order to intuitively analyze the mechanical properties of this binding structure, the morphological binding structure is simplified into partially superimposed structures step by step. Geometrically, two symmetrical rings are applied to constrain the radial displacement u and the axial displacement w, respectively. Then orthogonal rings are superposed on the front structure. Similarly, more complex rings can be superposed on the structure to approach more precise result. A binding structure with two-axisymmetric-rings as an example has the equilibrium equation as

$$\begin{aligned} \frac{\partial\sigma_r}{\partial r}+\frac{\partial\tau_z}{\partial z}+\frac{\sigma_r-\sigma_\theta}{r}=0 \\ \frac{\partial\sigma_z}{\partial z}+\frac{\partial\tau_{rz}}{\partial r}+\frac{\tau_{rz}}{r}=0 \end{aligned} \quad (10)$$

The radial displacement u and axial displacement w are the independent variables in the sphere. The corresponding strain components are

$$\varepsilon_r=\frac{\partial u}{\partial r},\quad \varepsilon_\theta=\frac{u}{r},\quad \varepsilon_z=\frac{\partial w}{\partial z},\quad \gamma_{zr}=\frac{\partial u}{\partial z}+\frac{\partial w}{\partial r} \quad (11)$$

The constitutive equation with the effect of concentration term is expressed as

$$\begin{cases} \varepsilon_r=\dfrac{1}{E}[\sigma_r-\nu(\sigma_\theta+\sigma_z)]+\dfrac{\Omega C}{3} \\ \varepsilon_\theta=\dfrac{1}{E}[\sigma_\theta-\nu(\sigma_z+\sigma_r)]+\dfrac{\Omega C}{3} \\ \varepsilon_z=\dfrac{1}{E}[\sigma_z-\nu(\sigma_r+\sigma_\theta)]+\dfrac{\Omega C}{3} \\ \gamma_{rz}=\dfrac{\tau_{rz}}{G}=\dfrac{2(1+\nu)}{E}\tau_{rz} \end{cases} \quad (12)$$

Combining eqs 10−12 obtains the Navier equation as

$$\begin{cases} \dfrac{1}{1-2\nu}\dfrac{\partial e}{\partial r}+\nabla^2u-\dfrac{u}{r^2}=-\dfrac{1}{2}\left(\dfrac{\nu}{1-2\nu}+\dfrac{1}{3}\right)\Omega\dfrac{dC(r)}{dr} \\ \dfrac{1}{1-2\nu}\dfrac{\partial e}{\partial z}+\nabla^2w=0 \end{cases} \quad (13)$$

where $\nabla^2=\frac{\partial^2}{\partial r^2}+\frac{1}{r}\frac{\partial}{\partial r}+\frac{\partial^2}{\partial z^2}$, $e=\varepsilon_r+\varepsilon_\theta+\varepsilon_z$ is the volumetric strain. The concentration $C(r,t)$ only changes with radial r at a time. This second-order homogeneous partial differential equation forms a *Boussinesq* problem and has the following solutions:

$$\begin{cases} u=A\dfrac{rz}{R^3}+B\dfrac{r}{R(R+z)}+C\dfrac{e^{\frac{r}{2\mu-1}}}{r}(-2\mu+r+1)\left[\int_0^r\dfrac{dC(r)}{r}dr+D\right] \\ w=A\left[\dfrac{z^2}{R^3}+(3-4\nu)\dfrac{1}{R}\right]+B\dfrac{1}{R}+E\int_0^r\dfrac{dC(r)}{r}dr \end{cases} \quad (14)$$

where C, D, and E are constants related to the concentration function $C(r)$. A and B are constants determined by boundary conditions: $R=\sqrt{r^2+z^2}$, $u=R_{radius}$, $z=\sqrt{2}/2R_{radius}$ on the spherical surface. Generally, the displacement boundary conditions are

$$\begin{aligned} u\left(u=\frac{\sqrt{2}}{2}R_{radius},\ z=\frac{\sqrt{2}}{2}R_{radius}\right)=R_{radius} \\ w\left(u=\frac{\sqrt{2}}{2}R_{radius},\ z=\frac{\sqrt{2}}{2}R_{radius}\right)=\frac{\sqrt{2}}{2}R_{radius} \end{aligned} \quad (15)$$

Substituting eq 15 into eq 14 obtains the constants:

$$\begin{aligned} A=\frac{(1+\sqrt{2})R_{radius}^2}{1-3\sqrt{2}+4\sqrt{2}\nu}, \\ B=\frac{R_{radius}^2(-13-6\sqrt{2}+8(2+\sqrt{2})\nu)}{2-6\sqrt{2}+8\sqrt{2}\nu} \end{aligned} \quad (16)$$

Then, four stress components are analytically obtained as

https://doi.org/10.1021/acsomega.2c06560
ACS Omega 2023, 8, 7492−7506

$$\begin{cases} \sigma_r = \dfrac{ER^2_{radius}}{1+\nu}\left[\dfrac{\left(-r^2+z^2+\dfrac{z^3}{\sqrt{r^2+z^2}}\right)\left(-13-6\sqrt{2}+8\left(2+\sqrt{2}\right)\nu\right)}{\left(r^2+z^2\right)\left(z+\sqrt{r^2+z^2}\right)^2\left(2-6\sqrt{2}+8\sqrt{2}\nu\right)}\right. \\ \left. -\dfrac{\left(1+\sqrt{2}\right)z\left(2r^2(1+\nu)+z^2(-1+2\nu)\right)}{\left(r^2+z^2\right)^{5/2}\left(1-3\sqrt{2}+4\sqrt{2}\nu\right)}\right]+G(C) \\ \sigma_\theta = \dfrac{ER^2_{radius}}{(\nu+1)\left(r^2+z^2\right)^{3/2}}\left\{\dfrac{\left[8\left(\sqrt{2}+2\right)\nu-6\sqrt{2}-13\right]\left(r^2+z^2\right)}{\left(8\sqrt{2}\nu-6\sqrt{2}+2\right)\left(\sqrt{r^2+z^2}+2\right)}+\dfrac{\left(\sqrt{2}+1\right)(1-2\nu)z}{4\sqrt{2}\nu-3\sqrt{2}+1}\right\} \\ +G(C) \\ \sigma_z = \dfrac{ER^2_{radius}\left\{\left[4\left(\sqrt{2}+3\right)\nu-4\sqrt{2}-11\right]r^2z+\left[4\left(\sqrt{2}+3\right)\nu+2\sqrt{2}-5\right]z^3\right\}}{2(\nu+1)\left(4\sqrt{2}\nu-3\sqrt{2}+1\right)\left(r^2+z^2\right)^{5/2}}+G(C) \\ \tau_{rz} = -\dfrac{ER^2_{radius}r\left\{r^2\left[-11-4\sqrt{2}+4\left(3+\sqrt{2}\right)\nu\right]+z^2\left[-5+2\sqrt{2}+4\left(3+\sqrt{2}\right)\nu\right]\right\}}{2\left(r^2+z^2\right)^{5/2}(1+\nu)\left(1-3\sqrt{2}+4\sqrt{2}\nu\right)} \end{cases} \quad (17)$$

where R_{radius} is the radius of the spherical electrode. $G(C) = w_G\int_0^r \frac{dC(r)}{r}dr$ is the concentration-related function and w_G is a constant. These stress expressions show that the stress is affected by a concentration-related function. It is noted that the above solution can be used for reference. For binding constraints, their effects can be calculated by the superposition method in elastic mechanics. The *Boussinesq* solution is suitable for this axisymmetric problem, while spherical harmonics function and superposition calculation can give analytical solutions for more general binding structures through some programming.[35] It is worth noting that this mechanical calculation for the binding structure is only suitable for specific materials with properties of strong oxidation for a tight binding, linear elasticity for a stable deformation and good electrical conductivity.

2.4. Hollow Core−Shell Structure. The solid core−shell protective structure is effective in a small volume change of the material caused by lithiation and delithiation, but for a material with a very large volume change rate, the hollow core−shell structure is more meaningful. If the matrix stiffness of the protective material is so large that the electrode material only deforms inward. The deformation may fill in the hollow part. Thus, the inner diameter a and outer diameter b of the core should satisfy the following geometric relation:

$$\frac{a}{b} = \left(\frac{\beta-1}{\beta}\right)^{1/3} \quad (18)$$

Here the volume expansion coefficient is $\beta V_{core} = V_{core} + V_{hollow}$. For silicon material, $\beta = 4$ and $a/b = (3/4)^{1/3}$. The boundary conditions of this model are

$$\begin{aligned} &u_c(r=b) = b \\ &\sigma_c(r=a) = 0 \\ &u_s(r=b) = b \\ &\sigma_{r,s}(r=b) = \sigma_{r,c}(r=b) \end{aligned} \quad (19)$$

Due to the high stiffness of the protective shell, here the displacement of the core−shell interface is ideally ignored. Simultaneously solving the eqs 1, 2, 5 and 19 obtains the analytical solution as

$$\begin{aligned} u_c = \frac{c_1}{r^2} + c_2 r + 9r^2\left(\lambda_c+2\mu_c\right)\left[9\lambda_c\int_0^r \frac{K(b)^3(3\lambda_c+2\mu_c)\Omega_c\frac{dC_c(r)}{dr}}{9(\lambda_c+2\mu_c)}dr\right. \\ \left. +18\mu_c\int_0^r \frac{K(b)^3(3\lambda_c+2\mu_c)\Omega_c\frac{dC_c(r)}{dr}}{9(\lambda_c+2\mu_c)}dr-\left[3r^3\lambda_c-2r^3\mu_c\right]c_c(r)\Omega_c\right] \end{aligned} \quad (20)$$

where c_1, c_2 are the integral constants introduced by the concentration function $C(r,t)$ and $u_c(r)$. They are determined by boundary conditions.

Finally, the radial stress on the core−shell boundary is obtained as

$$\begin{aligned} \sigma_r^{cs} = &\left[6\left(a^3+2b^3\right)\mu_c+9a^3\lambda_c\right]\left\{\left(8\mu_c^2\Omega_c+12\mu_c\lambda_c\Omega_c\right)\left[b^3\left(1+2\sum_{n=1}^{\infty}\frac{(-1)^n}{n\pi x_b}\sin(n\pi x_b)e^{-n^2\pi^2\tau}\right)\right.\right. \\ &\left.\bullet(C_R-C_0)+b^3C_0-a^3\left(1+2\sum_{n=1}^{\infty}\frac{(-1)^n}{n\pi x_a}\sin(n\pi x_a)e^{-n^2\pi^2\tau}\right)(C_R-C_0)-a^3C_0\right] \\ &+4\mu_c\frac{(3\lambda_c+2\mu_c)\Omega_c}{9}\bullet\left[9\int_a^b r^3(C_R-C_0)\left(\begin{matrix}\sum_{n=1}^{\infty}\frac{(-1)^{n+1}}{n\pi\sqrt{x}}\sin(n\pi x)e^{-n^2\pi^2\tau} \\ +2\sum_{n=1}^{\infty}\frac{(-1)^n}{n\pi x}\cos(n\pi x)e^{-n^2\pi^2\tau}\end{matrix}\right)dr-9a^3+9b^3\right]\Bigg\} \end{aligned} \quad (21)$$

This expression indicates that the stress increases with the increase of time and concentration.

2.5. Fracture Criterion. The core−shell interface has different fracturing mechanisms during charge−discharge processes.[39] The first one is the surface fracture caused by expansion. The second one is in the delithiation process that the volume shrinkage of the electrode causes the debonding of the core−shell interface. The key variables for fracturing are the hoop stress σ_T^s on the shell surface and the radial stress on the core−shell interface σ_r^{cs}. In order to quantify the fracture mechanism, the fracture energy release rate G_f and the debonding energy release rate G_d are introduced as[39]

$$G_f = Z\frac{(\overline{\sigma}_T^s)^2}{E_s}(b-a),\ G_d = \pi\frac{(\sigma_r^{cs})^2}{E_E}(b-a) \quad (22)$$

where $\overline{\sigma}_T^s = Z\int\int\int\sigma_T^s r^2\sin\phi dr d\theta/b^3 - a^3$ is the average hoop stress in the spherical shell and Z is a dimensionless coefficient for a *Griffith* crack. The elastic modulus of the spherical shell is E_s. $E_E = 1/(1/E_c + 1/E_s)$ is the effective elastic modulus at the core−shell interface, which is affected by the properties of the core−shell material. In the absence of a predetermined crack, Γ_f is the energy required for fracture and Γ_d is the energy required for core−shell interface debonding. Therefore, the energy criterion is G_f=Γ_f for surface fracture and G_d=Γ_d for interface debonding.

3. MODELING METHODOLOGY AND VALIDATION

The 3D models for the unprotected structure and three protective structures (binding protective structure, solid core−shell structure, and hollow core−shell structure) in Figure 1 will be numerically modeled. The detail relationship between the scale of shell−core and the mechanical performance of electrode has been depicted in the literature.[40] As a concrete computational example, in our model, the thickness of the shell or binding is set to 0.2 μm and the radius of electrode is set to 4 μm. In order to reduce the meshing calculation and supply a clear visualization, the thickness used here is not the same as the actual value in their experimental sample. The mechanical and electrochemical properties of the electrode will be analyzed during the charging process. This section will describe the modeling method and validate the simulation results.

https://doi.org/10.1021/acsomega.2c06560
ACS Omega 2023, 8, 7492−7506

3.1. Modeling Methodology and Computational Parameters. In this section, the numerical simulation models for the above structures will be set up and their partial differential equations composed of Fick's law and Navier equations will be numerically solved by finite element method. The diffusion process is simulated by the diluted matter transport module and the deformation is solved by the solid mechanics module.

In the four charging models, the initial concentration in the core domain is set to 11500 mol/m^3. This value is a half of the fully charged maximum concentration. Afterward, the inward flux from the outer surface is set to *in/Fa*, which is related to the charging current density and Faraday constant. For the protective structure, fully fixed constraints are set at the shell and binding structure to limit the deformation of the electrodes. The electrode material is assumed to be silicon in this study. The shell and binding as the protective structures are set to aluminum oxide and nano cellulose, respectively. The spherical electrode model without any protective structure is used as a reference to verify the influence of three protective structures on concentration and fracturing. The model parameters and variables are listed in Table 1. Figure 2 shows the mesh and boundary conditions of these four computational electrode models. This unprotected structure model was also simulated by Clerici et al.[41]

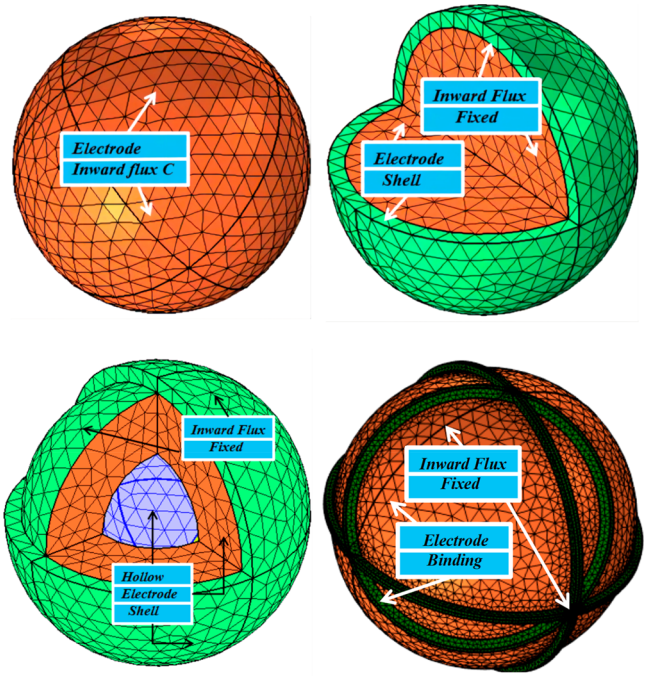

Figure 2. Geometry of four computational electrode models.

3.2. Validation of the Model. The numerical model is verified by the experimental data published by Clerici et al.[41] and Wu.[39] We simulated the charging process of a single particle with an unprotected structure and a solid core−shell structure, respectively. It is noted that the boundary conditions of the models in this paper are slightly different from those in the literature, where the fixed constraint was at the electrode center, while this paper sets the outer surface of the electrode as a fixed constraint.

Figure 3 depicts the radial stress and deformation at the interface. Unified color bar is used because each model is independent. It is clearly seen that the electrode expands with

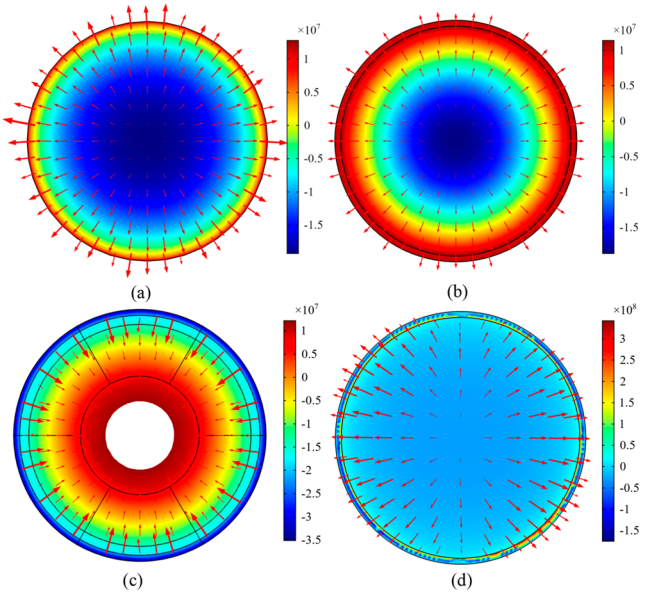

Figure 3. Radial stress and deformation at the interface of different models where (a)−(d) represent unprotected structure, core−shell structure, hollow core−shell structure and binding structure, respectively.

lithium intercalation during the charging process of the solid electrode model. Figures 3a and 3b depict that the presence of the shell structure creates a zero radial stress sphere inside the electrode and changes the direction of the radial stress. The arrows represent the radial displacement. It is observed that the shell structure effectively constrains the expansion of the particles. Figure 3c visually shows that the electrode material deforms toward the hollow portion rather than expands outward. Figure 3d shows that the radial stress at the binding interface is much higher than that inside the electrode.

Figure 4 shows the comparison between the theoretical calculations and experiment data. First, the rationality of geometrical settings is discussed. Figure 4a plots the fracture zone based on the criteria given by eq 22. Its gray area is the safety zone of the core−shell structure.[39] This figure provides a selection range on the size of the core−shell structure for fracturing or debonding free. Our computation sets the thickness of the shell or binding as 0.2 μm and the radius of electrode as 4 μm. Such geometrical settings refer to the criteria given by eq 22 and are shown in Figure 4a.

Further, Figures 4b-4e depict the comparison of the unprotected structure with the literature data when the initial SOC is 50% and the charging time is 200s. The dimensionless concentration, radial stress, hoop stress and Von Mises stress are used here. In Figure 4d, the evolution trend of radial stress is different from that in the literature, where the radial stress at the center is the largest and decreases to zero along the radius. In the theoretical derivation in eq 8, the center of the sphere is set as a fixed constraint, but this constraint cannot be set in the software. Therefore, the fixed constraints on the surface are set to meet the operation requirements of the software. The result shows that the radial stress on the outer surface of the model in this paper is not zero. For concentration, hoop stress and Von Mises stress, the model in this paper has the same changing trend as the data in the literature.

3.3. Validation of the Analytical Solutions. For the solid core−shell structure, eq 9 was selected to validate the

https://doi.org/10.1021/acsomega.2c06560
ACS Omega 2023, 8, 7492−7506

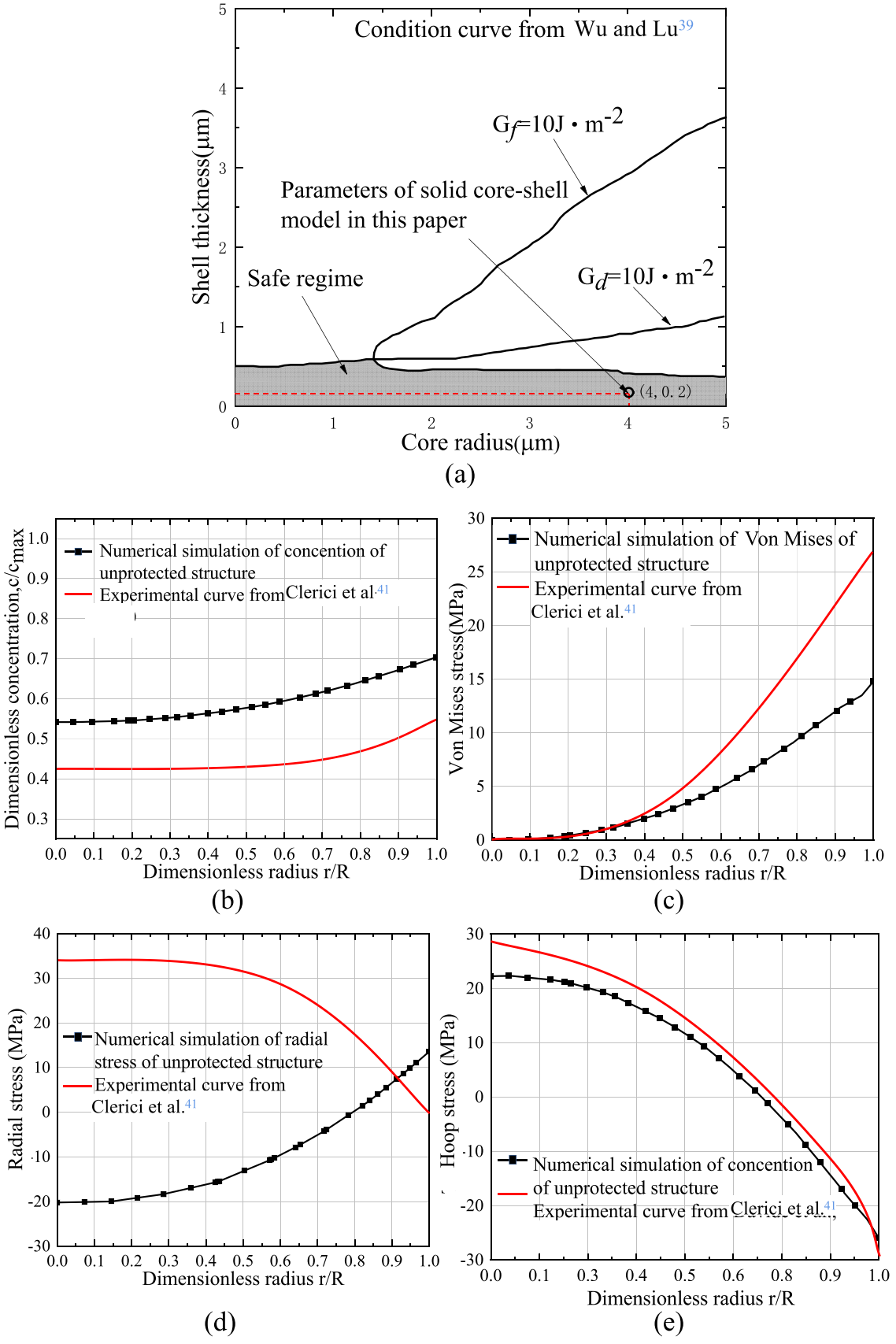

Figure 4. Geometric basis of the model and validation results ((a) The thickness of the solid core−shell structure is 0.2 μm, and the radius of the core is 4 μm referring to the condition curve digested from Wu and Lu;[39] (b) Lithium concentration, (c) Von Mises stress, (d) Radial stress, (e) Hoop stress at 200s during charging process for unprotected structure and digested data). Reprinted with permission from ref 39. Copyright 2017 American Chemical Society; Reprinted with permission from ref 41. Copyright 2020 Molecular Diversity Preservation International.

https://doi.org/10.1021/acsomega.2c06560
ACS Omega 2023, 8, 7492−7506

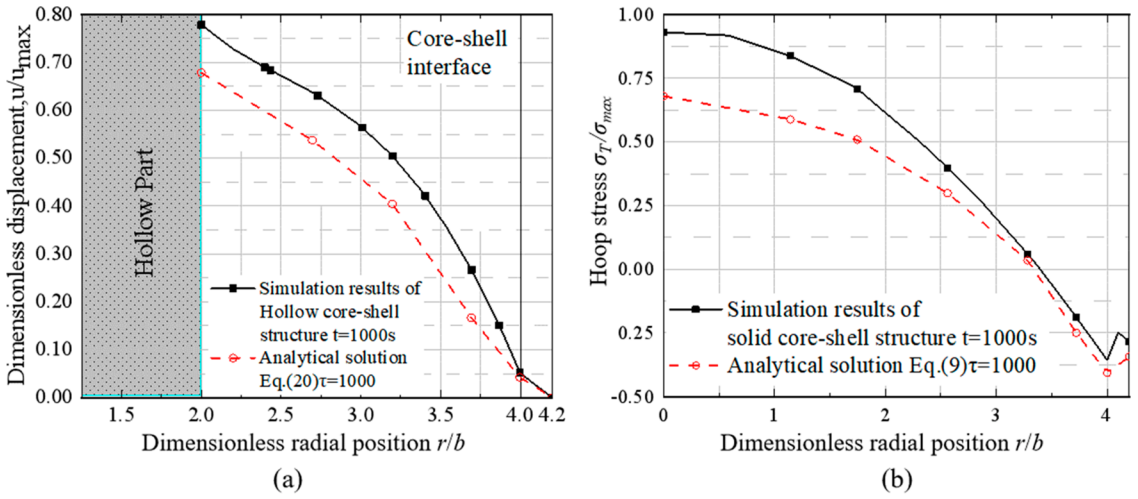

Figure 5. Verification of the analytical solutions ((a) with eq 20, (b) with eq 9).

practicability of the analytical solution. In eq 9, σ_T^s represents the surface hoop stress in different layers while the r is changing. The simulated concentration at 1000s was substituted in the expression of σ_T^s, then σ_T^s was normalized by the maximum value $\sigma_{T\max}^s$. It is observed that $1/r^3$ has a big impact on the computational result. Figure 5a plots the comparison between simulation and analytical result of dimensionless hoop stress. For the hollow core−shell structure, radial displacement was selected as the validated parameter due to its simplicity. The radial displacement at 1000s in the hollow core−shell model was substituted into eq 20 and its outputs are compared in Figure 5b. The data is normalized by the maximum value for dimensionless.

4. RESULTS AND DISCUSSION ON FRACTURING/ION TRANSMISSION

This section analyzes pros and cons of different models. The simulated dimensionless concentration, Von Mises stress, radial stress and hoop stress are presented in Figures 6a_1-6a_4 for the unprotected structure, in Figures 6b_1-6b_4 for the solid core−shell structure, in Figures 6c_1-6c_4 for the hollow core−shell structure and in Figures 6d_1-6d_4 for the binding structure. The effects of protective structures on ion transmission are comparatively analyzed and the effectiveness of antifracture is evaluated. For the binding structure, the fracture mechanism and optimization in both charging and discharging processes are further studied.

4.1. Performance of Ion Transmission. In this paper, the rate of ion transmission is expressed by dimensionless concentration and its gradient. The performances of ion transmission and fracturing will be discussed in charging process and discharging process, respectively.

4.1.1. Charging Process. In the simulation of charging process, the initial state of charge (SOC) of the electrode is set to 50% of the maximum concentration inside the electrode of 23000 mol/m^3. The ambient temperature is kept at 298 K. The total operation time is taken as 1000 s in the simulation. Figure 6a_1 shows the concentration of Li^+ trend graph of unprotected electrode along the radial direction at different charge time. The concentration of lithium ions is the largest on the outer surface and decreases in the radial direction to the center of the sphere. Comparison of Figure 6b_1, 6c_1 and 6d_1 observed that the SOC of the electrodes at the same charging time lower than that of the unprotected electrode. This is due to the lower ion permeability of the aluminum oxide protective coating. Therefore, fully charging the battery takes longer time and has more energy dissipation. Usually, the ion transmission rate is slower in the shell domain. When SOC is equal to 1, the electrode is fully charged and SOC cannot gain anymore.

Figure 7 plots stress fluctuation and contrast data for the models. Figure 7a is the concentration over time 0−1000 s at the point (2, 2, 2). The binding model has faster intercalation rate of the ions than the solid core−shell model. The lithium insertion rate of the hollow core−shell structure in Figure 7a is the fastest. This is because the binding structure exposes much larger area of the electrode surface and the electrode material is easier to transport ions than the protective shell material. The hollow core−shell structure is another form of nanotube materials. Its electrode is smaller and easier to insert lithium. This structure is suitable for the large volumetric strain of silicon and other electrodes. How large a hollow structure should be designed to improve the structural stability and ion permeability of the electrode is an interesting topic for further study.

Ion transmission is a complicated process in a battery system. When the battery is in charge, lithium ions are extracted from the lithium-containing compound in the positive electrode and move to the negative electrode through the electrolyte. Since the negative electrode has a layered structure with many micropores, the lithium ions reaching the negative electrode are inserted into the micropores of the carbon layer. The more lithium ions are inserted, the higher the charging capacity is.

4.1.2. Discharging Process. During the discharge process of the battery, the transport direction of ions and electrons is opposite to that in the charging process. In discharging, the lithium ions embedded in the negative electrode layer are released and return to the positive electrode. The more lithium ions return to the positive electrode, the higher the discharge capacity is. For the binding structure, only discharge is simulated. Its initial SOC is set to 1 and its initial conditions are the same as the charging process. Figure 8 shows the deformation at 0, 500, and 1000 s during the charging and discharging processes. The electrode expands during the lithium-ion intercalation process or the charging process. The electrode shrinks during the lithium-ion extraction process or the discharging process. In this figure, the darker the color on the electrode, the greater the degree of deformation. This means

https://doi.org/10.1021/acsomega.2c06560
ACS Omega 2023, 8, 7492−7506

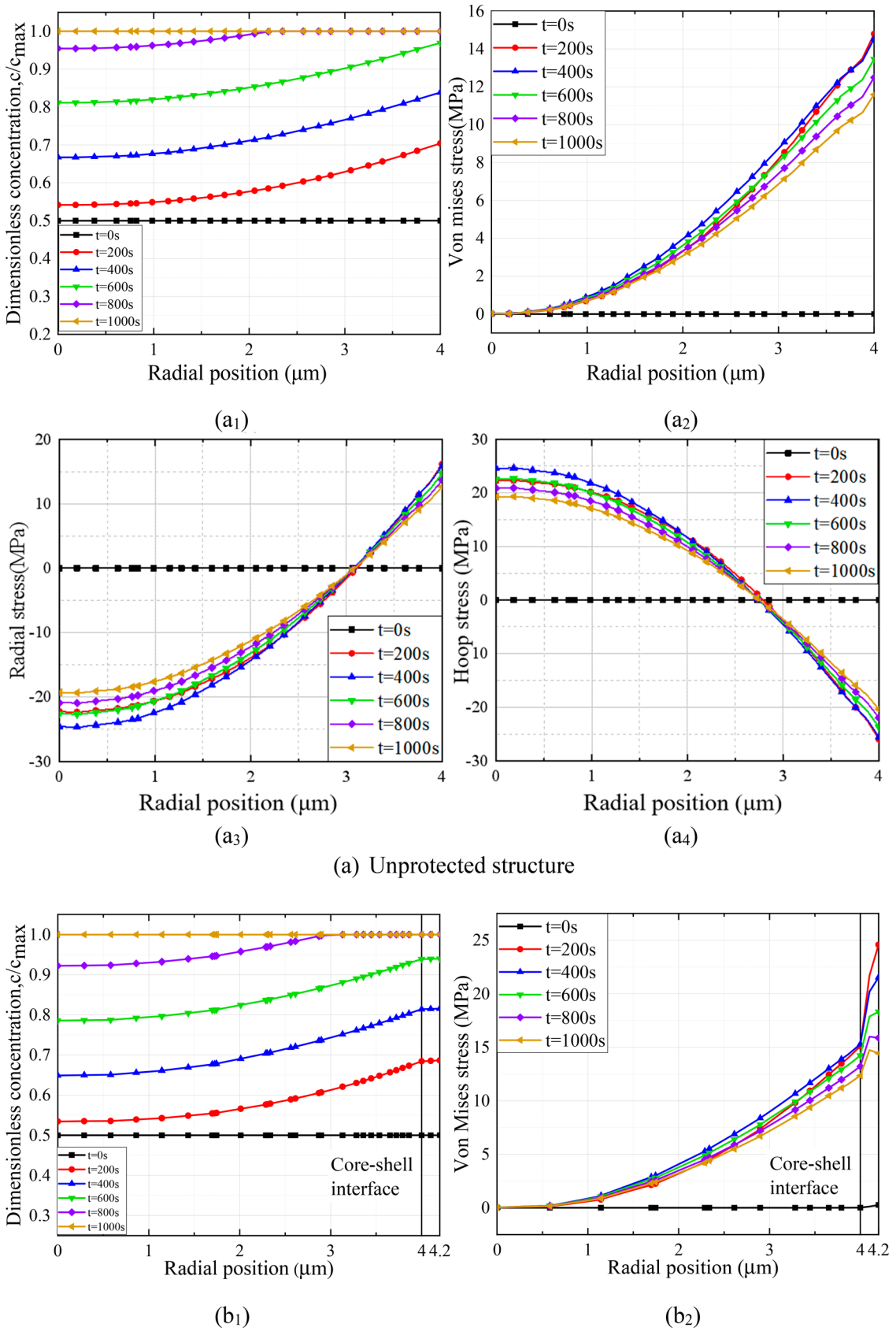

Figure 6. continued

https://doi.org/10.1021/acsomega.2c06560
ACS Omega 2023, 8, 7492−7506

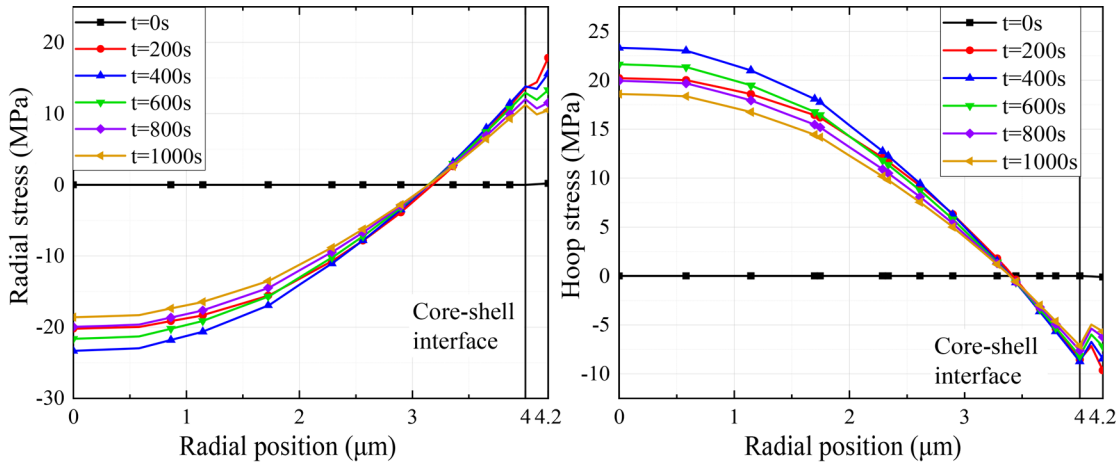

(b$_3$) (b$_4$)

(b) Solid core-shell structure

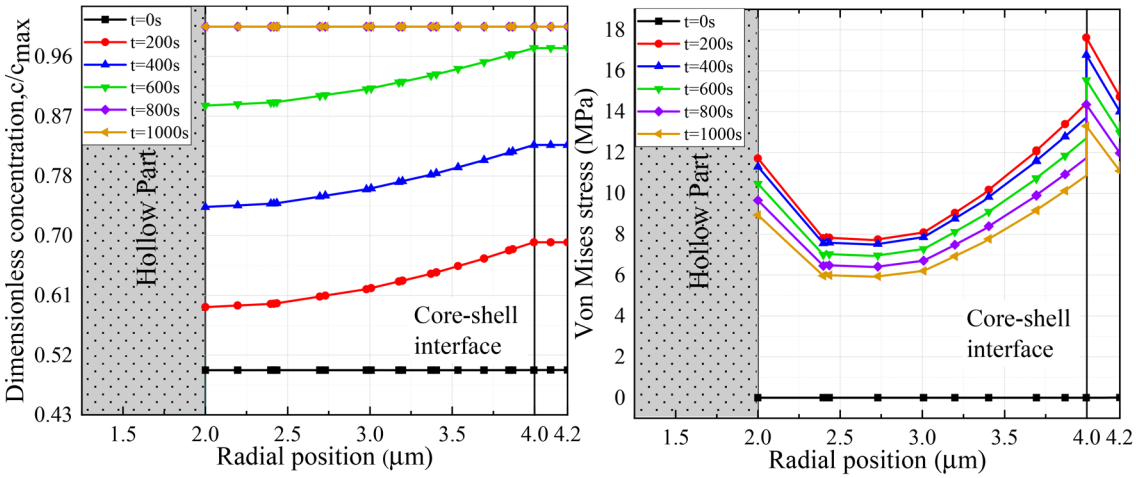

(c$_1$) (c$_2$)

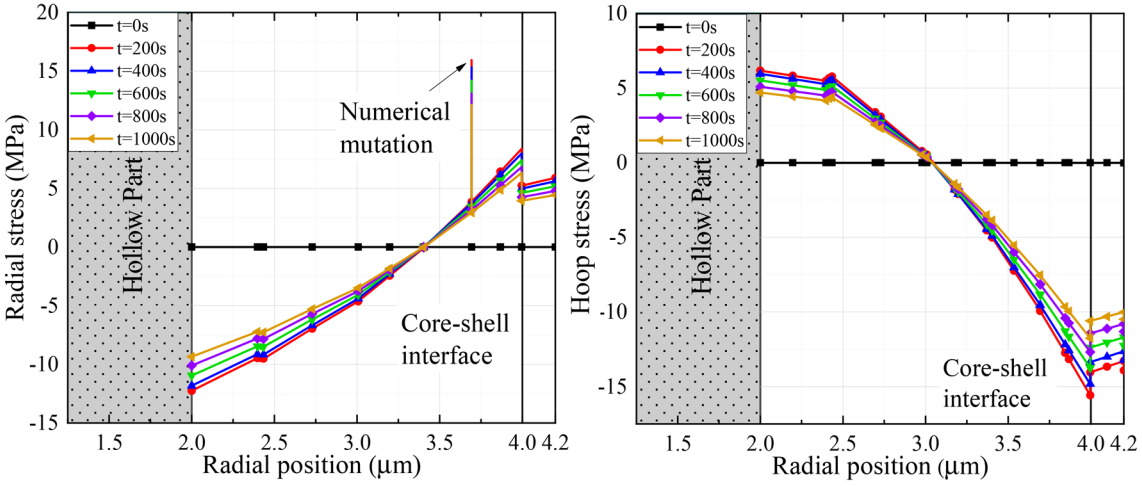

(c$_3$) (c$_4$)

(c) Hollow core-shell structure

Figure 6. continued

https://doi.org/10.1021/acsomega.2c06560
ACS Omega 2023, 8, 7492−7506

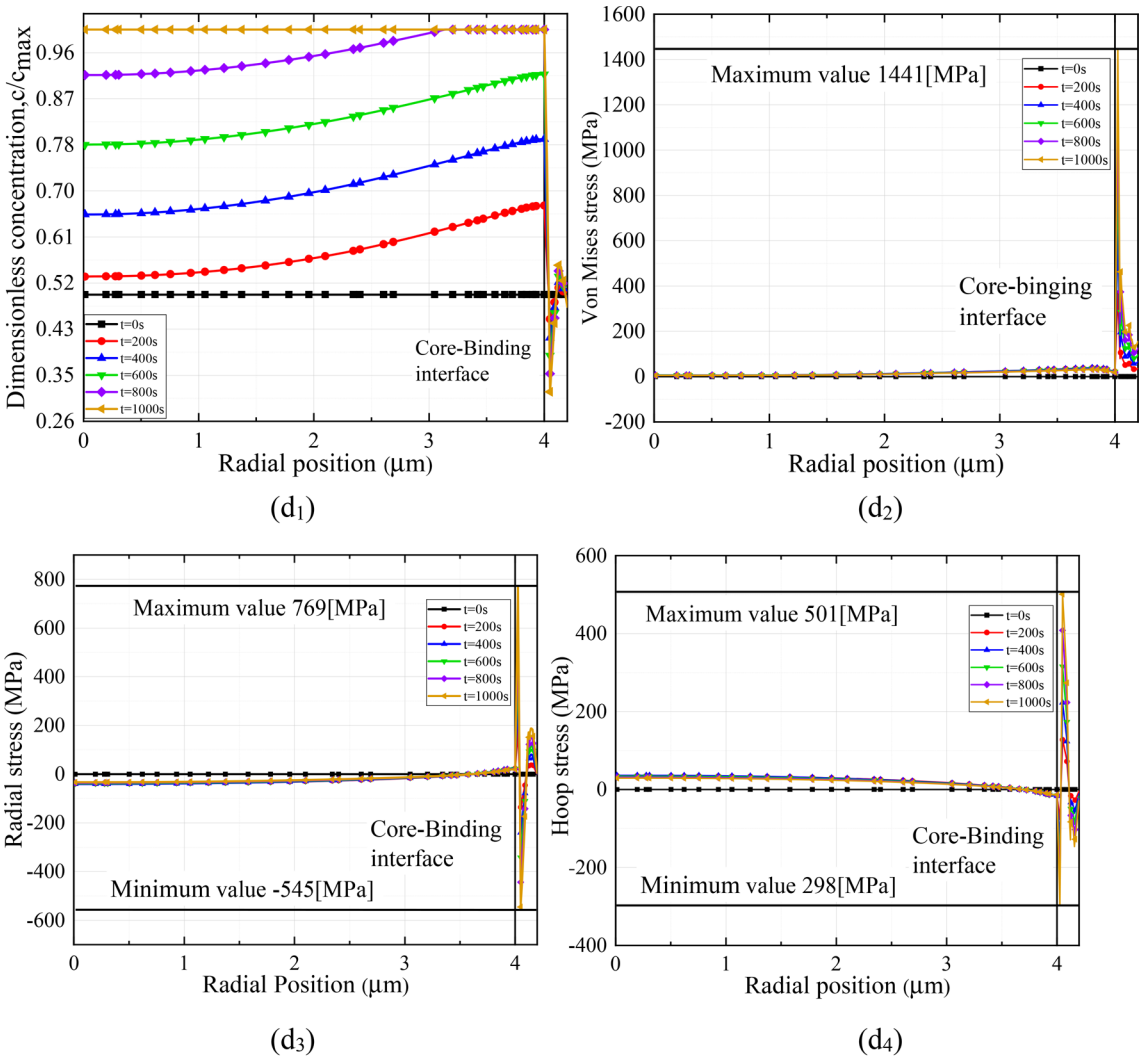

Figure 6. Evolution diagram of electrochemical parameters under constant current charging. ((a) for unprotected structure; (b) for solid core−shell structure; (c) for hollow core−shell structure; (d) for binding structure.).

that the ring-constraint provides a good constraint on the deformation in the area the ring covers.

Generally, the microstructures of the electrode are divided into cubic spinels, layered, and tubular forms. They allow three-dimensional, two-dimensional, and one-dimensional migration of ions, respectively. The ion migration rate slows down in the three electrode structures in turn, but is still faster than the rate in the shell structure. The ion transport rate of the bound structure is 2% slower than that of the unprotected structure. The density of binding constraints in the outer layer affects the ion permeability, as higher density results in slower ion transport. For the binding structure, further optimization is needed to obtain the best protection structure to achieve the characteristics of easy charging and high strength.

4.2. Performance of Antifracturing, Debonding, or Yielding Failure. *4.2.1. Fracturing on the Surface.* During the charging process of electrode, lithium ions are inserted into the layered electrode material and cause volume expansion. In the microstructure scale, the layered electrode material allows the deintercalation and intercalation of ions. When ions are embedded into the octahedral sites of alternating layers, the host atoms repel the intercalated ions. This leads to an increase in the distance between the layers and causes macroscopic expansion. The charging process in Figure 8 gives a macroscopic manifestation of Li-ion intercalation. In the process of swelling, the surface is mechanically subjected to hoop tensile stress and the inside of the electrode is mechanically subjected to compressive stress. A transition zone is observed along the radius direction from the sphere center, where the stress is very small and the zero position is near $r = 1/\sqrt{2}R$. Figures 6b$_3$, 6b$_4$ and Figures 6c$_3$, 6c$_4$ show that the shell structure can reduce the hoop tensile stress and radial compressive stress on the electrode surface. Figure 7b presents the shear stress near the surface at the charging time of 200, 600, and 1000 s, where the solid line is for the unprotected model and the dashed line is for the solid core−shell model. It is more clearly observed that the shell serves as an antifracture shelter. However, eq 9 shows that the hoop tensile stress on the surface of the shell leads to the fracture of protective structure, and the fracture is affected by the thickness of the shell. Thinner protective structure is more prone to surface fracture.

4.2.2. Yielding Failure. The Von Mises yield criterion states that the ductile material begins to yield when the shape-changed ratio of a certain point reaches a critical value. The Von Mises stress of the models in the radial direction over time is shown in

https://doi.org/10.1021/acsomega.2c06560
ACS Omega 2023, 8, 7492−7506

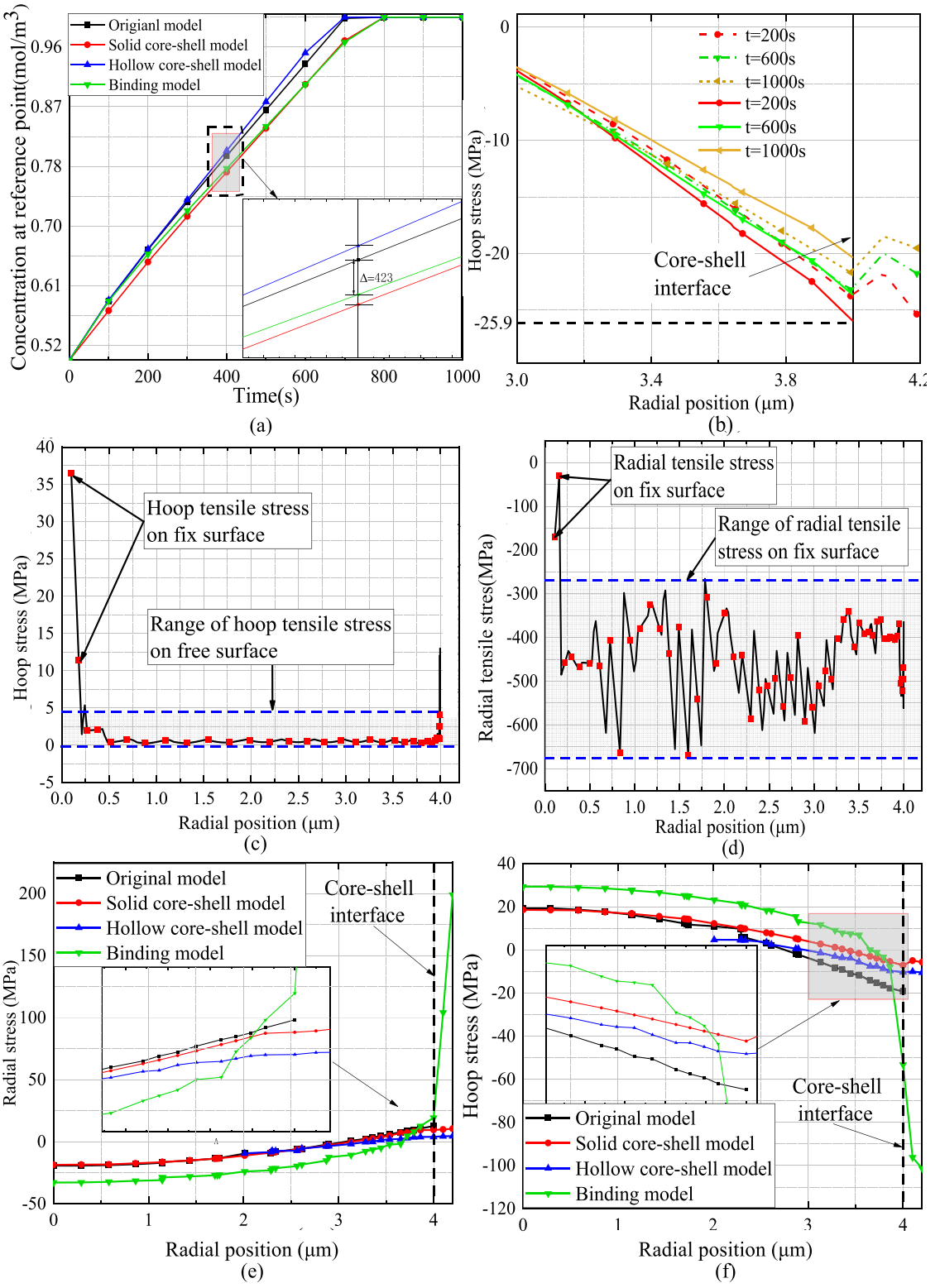

Figure 7. Parameter evolution and comparation of four structures ((a) The concentration graph over time 0−1000s at the point (2, 2, 2); (b) Hoop stress trend graph in unprotected and solid core−shell models during charging (solid line for unprotected model and dashed line for the solid core−shell model); (c) Hoop tensile stress diagram of the free surface of the binding model during charging; (d) Radial tensile stress diagram of the contact interface of the binding model during discharge; (e) Radial stress diagram of four structures; (f) Hoop stress diagram of four structures.).

Figures 6a_2, 6b_2, 6c_2 and 6d_2. The electrodes are mostly plastic materials. If the yielding failure is considered, the Von Mises stress can intuitively show the easily yielded location. The unprotected structure has the highest Von Mises stress on the electrode surface. The protective structure will have the abrupt changes in the Von Mises stress at the core−shell interface. During the charging process, the Von Mises stress will gradually decrease, because the lithium concentration inside the electrode

https://doi.org/10.1021/acsomega.2c06560
ACS Omega 2023, 8, 7492−7506

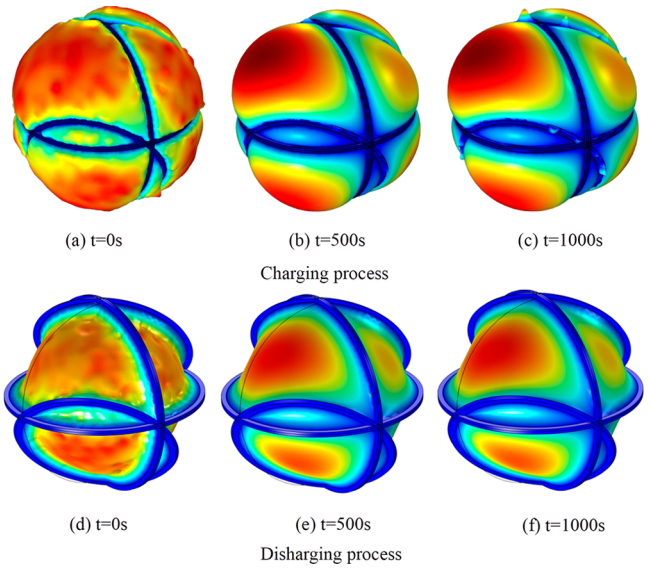

Figure 8. Deformation of the binding model at 0, 500, and 1000 s during charging and discharging.

increases and the decrease of the concentration gradient leads to the decrease of Von Mises stress. Therefore, the fracture of the electrode surface occurs at the beginning of the charge and discharge cycles.

Unlike the core−shell structure, the stress will change suddenly in the binding structure and is an order of magnitude higher as shown in Figures 6d_1-6d_4. Generally, the binding structure has high requirements on the performance of the binding material, such as high strength, high toughness, high stability, thermal shock resistance and stable chemical properties. Nanocellulose, as one ideal material for the binding, is a linear material with a certain aspect ratio with a diameter of nanometers. The micron-scale layered structure and nanothree-dimensional network structure of materials make the binding part have excellent physical and chemical properties. Therefore, the development of high-performance materials and structural design is the key to the electrode performance improvement.

4.2.3. Potential Debonding at Interface. During the discharging process of the electrode, the repulsive force between the host material and lithium ion is weakened when the ions are deintercalated. The reduction of repulsive force causes the shrinkage of layered material. The surface is mechanically subjected to hoop compressive stress and inward radial tensile stress. The discharging process in Figure 8 gives a macroscopic manifestation of Li-ion deintercalation. eq 20 indicates that thicker protective structure is more easily debonding. Figures 7c and 7d show that the radial and hoop stresses of the binding model fluctuate during charging and discharging. Figures 7e and 7f show the trends of radial/hoop stress in four structures. The radial tensile stress on the interface during discharge is much greater than tensile stress at the free surface during charging. If the critical values are $\Gamma_f = 10\ J{\cdot}m^{-2}$ and $\Gamma_d = 10\ J{\cdot}m^{-2}$, it is deduced that debonding is the main failure mode for the binding protective structure during a charge−discharge cycle. This conclusion is also true for the solid core−shell structure and the hollow core−shell structure. However, due to the flexibility and high ductility of the wire-like binding structure, debonding failure can be avoided by prestress. Figure 9 presents the aging mechanism of the electrodes in multiphysical environments and

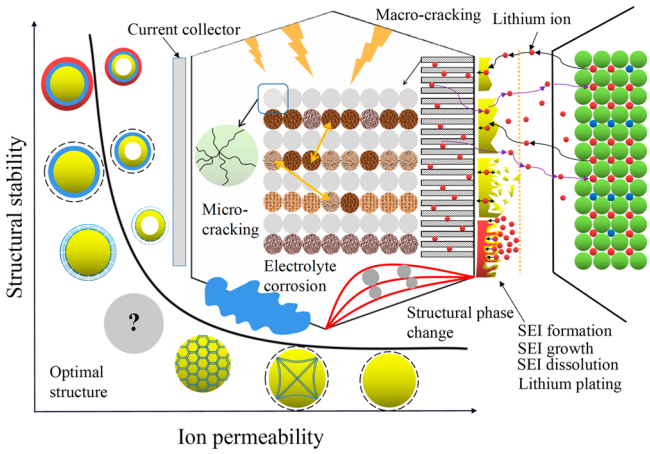

Figure 9. Electrode aging mechanism and protection strategy.

the properties of the protective structures, which include four circle-highlighted structures simulated in this paper.

Three aging mechanisms are identified for electrodes based on the location of aging. They are electrode surface aging, internal aging, and composite (current collector, binder, conductive addictive, etc.) aging. The outer protective structure of the electrode can effectively delay aging. The structures studied in this paper have unprotected structure, sparse binding structure, dense binding structure, core−shell structure and multilayer core−shell structure. However, their stability is negatively correlated with ionic permeability. In this perspective, well designing a novel binding structure to replace the shell structure can well balance the ion permeability and structural stability. In practice, the appropriate structure is selected according to the needs. If the safety is emphasized, the protective structure is strengthened or even using the double-layer shell. If conductivity is emphasized, the electrode should be exposed to more surface. Hence, the mechanical mechanism on the balance between stability and permeability can help us to provide a guidance for the selection of a proper structure for an electrode particle. The development of an analytical method can highly enhance the structural stability analysis.

5. CONCLUSIONS

This paper proposed a binding structure and comparatively investigated the performance of ion transmission and evaluated the fracturing risk of four spherical electrode protective structures of battery. Their governing equations and initial and boundary conditions for the coupling of concentration and stress were formulated. Two analytical solutions were obtained for the binding structure and the solid core−shell structure. The materials of the electrode and protective structure were set to silicon and aluminum oxide, respectively. The simulation models were validated with the experimental data available from literature. Finally, the ion transmission and fracturing risk are comparatively evaluated through numerical simulations. The following conclusions can be made from these investigations:

First, the binding structure has a 2% faster rate of ion insertion than solid core−shell structure and hollow core−shell structure but has 5% slower rate of ion insertion than the unprotected structure, thus prolonging charging time. Our models and analytical solutions can differentiate the performance among various electrode structures with certain materials. This study shows that compared with the unprotected structure, the binding structure reduces the hoop tensile stress on the

https://doi.org/10.1021/acsomega.2c06560
ACS Omega 2023, 8, 7492−7506

electrode surface, and thus effectively protects the electrode from charging expansion and fracturing. The binding structure with ring-constraints has less protection effect than the solid core−shell structure and has a sudden change of stress in the binding part. The binding structure has a superior performance if high-strength and high-toughness materials are used as the binding wires.

Second, the solid core−shell structure can effectively prevent the electrode surface from fracturing, thus being the most widely used electrode protection structure. The solid core−shell structure has the slowest charging rate and the most energy dissipation.

Third, the stress is alternative during a charging−discharging cycle. The radial stress at the interface between the core and the protective structure in the hollow core−shell structure is smaller than that of the binding structure. The hollow part can provide a deformation space for the electrode material.

AUTHOR INFORMATION

Corresponding Author

J. G. Wang − *School of Mechanics and Civil Engineering and State Key Laboratory for Geomechanics and Deep Underground Engineering, China University of Mining and Technology, Xuzhou 221116, China;* orcid.org/0000-0003-2988-7867; Email: jgwang@cumt.edu.cn, nuswjg@yahoo.com

Authors

Qi Liu − *School of Mechanics and Civil Engineering, China University of Mining and Technology, Xuzhou 221116, China*

Bowen Hu − *State Key Laboratory for Geomechanics and Deep Underground Engineering and School of Mechanics and Civil Engineering, China University of Mining and Technology, Xuzhou 221116, China*

Complete contact information is available at: https://pubs.acs.org/10.1021/acsomega.2c06560

Notes

The authors declare no competing financial interest.

ACKNOWLEDGMENTS

The authors are grateful for the financial support from the National Natural Science Foundation of China (Grant No. 51674246, 42030810).

REFERENCES

(1) Duffner, F.; Kronemeyer, N.; Tubke, J.; Leker, J.; Winter, M.; Schmuch, R. Post-Lithium-Ion Battery Cell Production and Its Compatibility with Lithium-Ion Cell Production Infrastructure. *Nat. Energy* **2021**, *6*, 123−134.

(2) Zhou, X. D.; Reimuth, C.; Xu, B. X. Phase-Field Simulation of Misfit Dislocations in Two-Phase Electrode Particles: Driving Force Calculation and Stability Analysis. *Int. J. Solids Struct.* **2022**, *249*, 111688.

(3) Carlstedt, D.; Runesson, K.; Larsson, F.; Tu, V.; Janicke, R.; Asp, L. E. Computational Modelling of Structural Batteries Accounting for Stress-Assisted Convection in the Electrolyte. *Int. J. Solids Struct.* **2022**, *238*, 111343.

(4) Hasan, M. K.; Mahmud, M.; Ahasan Habib, A. K. M.; Motakabber, S. M. A.; Islam, S. Review of Electric Vehicle Energy Storage and Management System: Standards, Issues, and Challenges. *J. Energy Storage* **2021**, *41*, 102940.

(5) Li, J. H.; Wu, J.; Yu, Y. X. Toward Large-Capacity and High-Stability Lithium Storages Via Constructing Quinone-2d-Mno2-Pillared Structures. *J. Phys. Chem. C* **2021**, *125*, 3725−3732.

(6) Ucel, I. B.; Gudmundson, P. A Statistical Rve Model for Effective Mechanical Properties and Contact Forces in Lithium-Ion Porous Electrodes. *Int. J. Solids Struct.* **2022**, *244*, 111602.

(7) Chen, Y. Q.; Kang, Y. Q.; Zhao, Y.; Li, Y. X.; Wang, L.; Liu, J. L.; et al. A Review of Lithium-Ion Battery Safety Concerns: The Issues, Strategies, and Testing Standards. *J. Energy Chem.* **2021**, *59*, 83−99.

(8) Gao, X.; Lu, W. Q.; Xu, J. Unlocking Multiphysics Design Guidelines on Si/C Composite Nanostructures for High-Energy-Density and Robust Lithium-Ion Battery Anode. *Nano Energy* **2021**, *81*, 105591.

(9) Kizzire, D. G.; Richter, A. M.; Harper, D. P.; Keffer, D. J. Lithium and Sodium Ion Binding Mechanisms and Diffusion Rates in Lignin-Based Hard Carbon Models. *Acs Omega* **2021**, *6*, 19883−19892.

(10) As, A.; Icn, A.; Ps, B. Performance Degradation Due to Anodic Failure Mechanisms in Lithium-Ion Batteries. *J. Power Sources* **2020**, *502*, 229145.

(11) Schiele, A.; Breitung, B.; Mazilkin, A.; Schweidler, S.; Janek, J.; Gumbel, S.; Fleischmann, S.; Burakowska-Meise, E.; Sommer, H.; Brezesinski, T. Silicon Nanoparticles with a Polymer-Derived Carbon Shell for Improved Lithium-Ion Batteries: Investigation into Volume Expansion, Gas Evolution, and Particle Fracture. *Acs Omega* **2018**, *3*, 16706−16713.

(12) Azam, M. A.; Safie, N. E.; Ahmad, A. S.; Yuza, N. A.; Zulkifli, N. S. A. Recent Advances of Silicon, Carbon Composites and Tin Oxide as New Anode Materials for Lithium-Ion Battery: A Comprehensive Review. *J. Energy Storage* **2021**, *33*, 102096.

(13) Wang, Q. S.; Meng, T.; Li, Y. H.; Yang, J. D.; Huang, B. B.; Ou, S. Q.; Meng, C. G.; Zhang, S. Q.; Tong, Y. X. Consecutive Chemical Bonds Reconstructing Surface Structure of Silicon Anode for High-Performance Lithium-Ion Battery. *Energy Storage Mater.* **2021**, *40*, 499−499.

(14) Yuan, C. H.; Gao, X.; Jia, Y. K.; Zhang, W.; Wu, Q. L.; Xu, J. Coupled Crack Propagation and Dendrite Growth in Solid Electrolyte of All-Solid-State Battery. *Nano Energy* **2021**, *86*, 106057.

(15) Rage, B.; Delbegue, D.; Louvain, N.; Lippens, P. E. Engineering of Silicon Core-Shell Structures for Li-Ion Anodes. *Chem.—Eur. J.* **2021**, *27*, 16275−16290.

(16) Cao, Z. G.; Yang, Y. B.; Qin, J. L.; Su, Z. X. A Core-Shell Porous Mno2/Carbon Nanosphere Composite as the Anode of Lithium-Ion Batteries. *J. Power Sources* **2021**, *491*, 229577.

(17) Su, L. W.; Jing, Y.; Zhou, Z. Li Ion Battery Materials with Core-Shell Nanostructures. *Nanoscale* **2011**, *3*, 3967−3983.

(18) Gao, J. T.; Wang, X. C.; Huang, Y. D.; Meng, Z. T.; Sun, Y.; Zhang, Y.; Guo, Y.; Tang, X. C. Hollow Core-Shell Structured Cnt/Pan@Co9s8@C Coaxial Nanocables as High-Performance Anode Material for Lithium-Ion Batteries. *J. Alloys Compd.* **2021**, *853*, 157354.

(19) Sedlatschek, T.; Lian, J. H.; Li, W.; Jiang, M. L.; Wierzbicki, T.; Bazant, M. Z.; Zhu, J. E. Large-Deformation Plasticity and Fracture Behavior of Pure Lithium under Various Stress States. *Acta Mater.* **2021**, *208*, 116730.

(20) Yang, Z. W.; et al. A Unique Structure of Highly Stable Interphase and Self-Consistent Stress Distribution Radial-Gradient Porous for Silicon Anode. *Adv. Funct. Mater.* **2022**, *32*, 2107897.

(21) Qiao, Y. Q.; et al. In Situ Observation of the Electrochemical Lithiation of a Single Mno@C Nanorod Electrode with Core/Shell Structure. *Chem. Commun.* **2022**, *58*, 879−882.

(22) Chen, Y. X.; Sang, M. S.; Jiang, W. J.; Wang, Y.; Zou, Y. L.; Lu, C. S.; Ma, Z. S. Fracture Predictions Based on a Coupled Chemo-Mechanical Model with Strain Gradient Plasticity Theory for Film Electrodes of Li-Ion Batteries. *Eng. Fract. Mech.* **2021**, *253*, 107866.

(23) Hao, W. F.; Yuan, Z. R.; Li, D. D.; Zhu, Z. Y.; Jiang, S. P. Study on Mechanical Properties and Failure Mechanism of 18650 Lithium-Ion Battery Using Digital Image Correlation and Acoustic Emission. *J. Energy Storage* **2021**, *41*, 102894.

(24) Wang, X.; Wu, Q.; Li, S. Y.; Tong, Z. M.; Wang, D.; Zhuang, H. L. L.; Wang, X. Y.; Lu, Y. Y. Lithium-Aluminum-Phosphate Coating

Enables Stable 4.6 V Cycling Performance of Licoo2 at Room Temperature and Beyond. *Energy Storage Mater.* **2021**, *37*, 67−76.
(25) Wu, Q. C.; Yu, R.; Zhou, Z. H.; Liu, H. W.; Jiang, R. L. Encapsulation of a Core-Shell Porous Fe3o4@Carbon Material with Reduced Graphene Oxide for Li+ Battery Anodes with Long Cyclability. *Langmuir* **2021**, *37*, 785−792.
(26) Lin, X.-M.; Ni, J.-C.; Zhan, F.-P.; Huang, X.-G.; Chen, G.-L.; Wang, Q.-X. Lithium-Storage Performance and Mechanism of a (Ni0.5co0.5)(9)S-8@Nc Hollow Nanocube Composite as an Advanced Anode. *J. Phys. Chem. C* **2021**, *125*, 26363−26370.
(27) Cho, B.; Lim, H.; Lee, H. N.; Park, Y. M.; Kim, H.; Kim, H. J. High-Capacity and Cycling-Stable Polypyrrole-Coated Mwcnt@ Polyimide Core-Shell Nanowire Anode for Aqueous Rechargeable Sodium-Ion Battery. *Surf. Coat. Technol.* **2021**, *407*, 126797.
(28) Chen, H. H.; Ke, G. X.; Wu, X. C.; Li, W. Q.; Mi, H. W.; Li, Y. L.; Sun, L. N.; Zhang, Q. L.; He, C. X.; Ren, X. Z. Carbon Nanotubes Coupled with Layered Graphite to Support Snte Nanodots as High-Rate and Ultra-Stable Lithium-Ion Battery Anodes. *Nanoscale* **2021**, *13*, 3782−3789.
(29) Sun, J. T.; et al. Core-Shell Structure of a Polypyrrole-Coated Phosphorus/Carbon Nanotube Anode for High-Performance Lithium-Ion Batteries. *ACS Appl. Energy Mater.* **2021**, *4*, 4112−4118.
(30) Salah, M.; Hall, C.; Murphy, P.; Francis, C.; Kerr, R.; Stoehr, B.; Rudd, S.; Fabretto, M. Doped and Reactive Silicon Thin Film Anodes for Lithium-Ion Batteries: A Review. *J. Power Sources* **2021**, *506*, 230194.
(31) Hyun, J. I.; Kong, K.; Choi, S.; Na, M. Y.; Kim, K. B.; Kim, W. T.; Kim, D. Synthesis of Porosity Controllable Nanoporous Silicon with a Self-Coated Nickel Layer for Lithium-Ion Batteries. *J. Power Sources* **2021**, *495*, 229802.
(32) Prussin, S. Generation and Distribution of Dislocations by Solute Diffusion. *J. Appl. Phys.* **1961**, *32*, 1876−1881.
(33) Di Leo, C. V.; Rejovitzky, E.; Anand, L. Diffusion-Deformation Theory for Amorphous Silicon Anodes: The Role of Plastic Deformation on Electrochemical Performance. *Int. J. Solids Struct.* **2015**, *67−68*, 283−296.
(34) Anand, L. A Cahn−Hilliard-Type Theory for Species Diffusion Coupled with Large Elastic-Plastic Deformations. *J. Mech. Phys. Solids* **2012**, *60*, 1983−2002.
(35) Constantinescu, A.; Korsunsky, A. *Elasticity with Mathematica: An Introduction to Continuum Mechanics and Linear Elasticity* **2007**, 1−255.
(36) Wang, Y.; Wu, H.; Sun, L. Z.; Jiang, W. J.; Lu, C. S.; Ma, Z. S. Coupled Electrochemical-Mechanical Modeling with Strain Gradient Plasticity for Lithium-Ion Battery Electrodes. *Eur. J. Mech. Solids* **2021**, *87*, 104230.
(37) Zhao, K. J.; Pharr, M.; Vlassak, J. J.; Suo, Z. G. Fracture of Electrodes in Lithium-Ion Batteries Caused by Fast Charging. *J. Appl. Phys.* **2010**, *108*, 073517.
(38) Cheng, Y. T.; Verbrugge, M. W. Evolution of Stress within a Spherical Insertion Electrode Particle under Potentiostatic and Galvanostatic Operation (Vol 190, Pg 453, 2009). *J. Power Sources* **2011**, *196*, 2430−2431.
(39) Wu, B.; Lu, W. Mechanical Modeling of Particles with Active Core-Shell Structures for Lithium-Ion Battery Electrodes. *J. Phys. Chem. C* **2017**, *121*, 19022−19030.
(40) Zhao, K. J.; Pharr, M.; Hartle, L.; Vlassak, J. J.; Suo, Z. G. Fracture and Debonding in Lithium-Ion Batteries with Electrodes of Hollow Core-Shell Nanostructures. *J. Power Sources* **2012**, *218*, 6−14.
(41) Clerici, D.; Mocera, F.; Soma, A. Analytical Solution for Coupled Diffusion Induced Stress Model for Lithium-Ion Battery. *Energies* **2020**, *13*, 1717.
(42) Guo, H. J.; Li, X. H.; Zhang, X. M.; Wang, H. Q.; Wang, Z. X.; Peng, W. J. Diffusion Coefficient of Lithium in Artificial Graphite, Mesocarbon Microbeads, and Disordered Carbon. *New Carbon Mater.* **2007**, *22*, 7−11.
(43) Barai, P.; Mukherjee, P. P. Stochastic Analysis of Diffusion Induced Damage in Lithium-Ion Battery Electrodes. *J. Electrochem. Soc.* **2013**, *160*, A955−A967.
(44) Christensen, J. Modeling Diffusion-Induced Stress in Li-Ion Cells with Porous Electrodes. *J. Electrochem. Soc.* **2010**, *157*, A366−A380.
(45) *Aluminum Oxide Al_2O_3 Ceramic Properties*. https://accuratus.com/alumox.html.

https://doi.org/10.1021/acsomega.2c06560
ACS Omega 2023, 8, 7492−7506